Interactions between terminal ribosomal RNA helices stabilize the *E. coli* large ribosomal subunit

AMOS J. NISSLEY,[1] TAMMAM S. KAMAL,[2] and JAMIE H.D. CATE[1,2,3]

[1]Department of Chemistry, University of California, Berkeley, Berkeley, California 94720, USA

[2]Department of Molecular and Cell Biology, University of California, Berkeley, Berkeley, California 94720, USA

[3]Molecular Biophysics and Integrated Bioimaging Division, Lawrence Berkeley National Laboratory, Berkeley, California 94720, USA

ABSTRACT

The ribosome is a large ribonucleoprotein assembly that uses diverse and complex molecular interactions to maintain proper folding. In vivo assembled ribosomes have been isolated using MS2 tags installed in either the 16S or 23S ribosomal RNAs (rRNAs), to enable studies of ribosome structure and function in vitro. RNA tags in the *Escherichia coli* 50S subunit have commonly been inserted into an extended helix H98 in 23S rRNA, as this addition does not affect cellular growth or in vitro ribosome activity. Here, we find that *E. coli* 50S subunits with MS2 tags inserted in H98 are destabilized compared to wild-type (WT) 50S subunits. We identify the loss of RNA–RNA tertiary contacts that bridge helices H1, H94, and H98 as the cause of destabilization. Using cryogenic electron microscopy (cryo-EM), we show that this interaction is disrupted by the addition of the MS2 tag and can be restored through the insertion of a single adenosine in the extended H98 helix. This work establishes ways to improve MS2 tags in the 50S subunit that maintain ribosome stability and investigates a complex RNA tertiary structure that may be important for stability in various bacterial ribosomes.

Keywords: bacterial ribosomes; rRNA; cryo-EM

INTRODUCTION

The ribosome is a large ribonucleoprotein assembly responsible for protein synthesis in the cell. Due to its complexity, the ribosome is composed of intricate networks of RNA–protein and RNA–RNA interactions (Noller 2005). These complex interactions are formed during ribosome assembly, which is a process requiring ribosomal RNA (rRNA), ribosomal proteins (rProteins), and many auxiliary assembly factors (Shajani et al. 2011). In *Escherichia coli* (*E. coli*), the three rRNAs—5S, 16S, and 23S—are all transcribed as a single transcript. During the early stages of ribosomal large subunit (LSU) assembly, sequences flanking the 5′ and 3′ ends of the pre-23S rRNA transcript base-pair to form the leader trailer (LT) helix (Liiv and Remme 1998). The LT helix is then subsequently cleaved by several RNases, and the remaining RNA helix comprises helix 1 (H1) of the pre-23S rRNA (Nikolaev et al. 1973; Ginsburg and Steitz 1975; Li et al. 1999). Additionally, it has been shown that some bacteria remove H1 post-assembly and this removal is correlated with the evolutionary loss of H98 (Shatoff et al. 2021), which suggests a synergistic role between the two helices.

The use of affinity tags in the 23S rRNA has enabled the in vitro study of in vivo assembled LSUs with mutations in 23S rRNA. This has commonly been achieved through the insertion of an RNA helix from the genome of the MS2 bacteriophage into helix H98 of the 23S rRNA on the surface of the ribosome (Youngman and Green 2005). Tagged mutant ribosomal subunits can then be purified using the MS2 coat protein dimer that selectively binds to the MS2 RNA helix (Peabody 1993). MS2 tags inserted in H98 of 23S rRNA have been used extensively to enable the investigation of rRNA function (Youngman et al. 2004; Lancaster et al. 2008), in engineered ribosomes (Ward et al. 2019), and for in vivo ribosome tracking (Metelev et al. 2022). Although *E. coli* 50S ribosomal subunits with MS2 tags inserted into H98 retain wild-type (WT) in vivo and in vitro function, we previously showed that these 50S subunits have lower thermostability compared to WT 50S subunits (Nissley et al. 2023).

Here, we investigate the loss of thermostability in the *E. coli* LSU upon the addition of an MS2 tag into H98. We find that RNA contacts between nucleotides at the interface of rRNA helices H1, H94, and H98 are important for the stability of the *E. coli* 50S ribosomal subunit. Using

cryogenic electron microscopy (cryo-EM), we show that this interaction is disrupted by the addition of previous MS2 tag designs in H98 and that the addition of a single adenosine residue in the tag can restore the tertiary interaction and WT levels of stability. The MS2 tags described herein offer an improved method for studying mutant and engineered ribosomes without the introduction of additional instability. Moreover, tertiary interactions between helices at the terminal ends of 23S rRNA corresponding to H1, H94, and H98 are found in many bacteria and these likely play stabilizing roles in a variety of bacterial ribosomes.

RESULTS AND DISCUSSION

H1, H94, and H98 interact in the *E. coli* LSU

To better understand the architecture of the region surrounding H98, we examined the structure of the *E. coli* ribosome (Watson et al. 2020). Helices H1, H94, and H98 reside on the surface of the 50S ribosomal subunit, and the apical regions of H1 and H98 extend away from the ribosome (Fig. 1A). H1 is formed through base-pairing between the 5′ and 3′ ends of the 23S rRNA (nucleotides 1–8 and 2895–2904, respectively). The 3′ end of 23S rRNA comprises Domain VI of the LSU which contains RNA helices H94–H101. In the *E. coli* ribosome, H1, H94, and H98 are in close proximity (Fig. 1B), and nucleotides at the base of H1 (G9, A10), the base of H94 (U2629), and in the apical loop of H98 (A2800) form tertiary interactions.

The purification of *E. coli* LSUs with mutations in 23S rRNA has commonly been achieved through the insertion of MS2 tags into H98. The original sequence of the MS2 tag from Youngman and Green (2005) is shown in Figure 2A (referred to here as MS2-V1). The tag is inserted into H98 by extension of the helix, which culminates with a polyuridine stretch (RNA linker). The MS2 helix is then inserted at the end of the RNA linker to ensure that it is accessible to the MS2 coat protein. A second tag design, which includes a different linker sequence and mutations in the MS2 stem–loop that increase the MS2 coat protein's affinity for the RNA (Lowary and Uhlenbeck 1987), was used more recently (Ward et al. 2019) (referred to here as MS2-V2).

It was previously shown that 50S subunits with an MS2-V2 tag inserted into H98 are destabilized compared to WT subunits (Nissley et al. 2023). We hypothesized that the insertion of an MS2 tag into H98 disrupts the tertiary interactions between H1, H94, and H98 and causes global destabilization of the 50S subunit. In the WT ribosome structure, nucleotide A2800 in H98 interacts with bases near H1, bridging H1 and H98. Although A2800 is not removed during the insertion of MS2-V1 or V2, the extension of the helix and the loss of A2799 in the H98 apical loop could drive A2800 into a Watson–Crick base pair with U2796 in the H98 helix rather than remaining flipped out to interact with H1 and H94. To test whether we could improve the MS2 tag design, we added an additional adenosine into a position synonymous to A2800 (MS2-V3). This design would allow the additional unpaired adenosine to interact with H1 nucleotides and restore the canonical structure of this region.

MS2-V3 restores stability to the *E. coli* LSU

To test whether the loss of A2800 in MS2 tags was the cause for destabilization of the 50S subunit, we tested the activity of 50S subunits with MS2-V1, V2, or V3 tags using an in vitro nanoluciferase (nLuc) translation assay. As was shown previously, the insertion of an MS2-V1 tag does not affect in vitro ribosome activity at 37°C (Fig. 2B; Youngman and Green 2005; Ward et al. 2019). We observe a slight decrease in the activity of 50S subunits with MS2-V2 tags; however, this may be due to the additional incubation step at 37°C before the in vitro translation assay (Materials and Methods). Notably, 50S subunits with an MS2-V3 insertion have similar levels of activity to untagged WT 50S subunits.

While ribosome activity at 37°C is not affected by the insertion of MS2 tags in H98, we also investigated the ability of 50S subunits to withstand a heat treatment step before the in vitro translation assays. After preincubation at 60°C, subunits with MS2-V1 and V2 inserted in H98 exhibit only 18% and 11%, respectively, of the activity of untagged WT subunits (Fig. 2C). This indicates that subunits with MS2-V1 and V2 tags are destabilized compared to WT subunits. In contrast, 50S subunits with MS2-V3 tags demonstrate WT levels of activity after incubation at 60°C (Fig. 2C; Supplemental Fig. S1). This suggests that loss of the A2800 interaction plays a role in the destabilization of subunits with MS2-V1 and MS2-V2 tags.

We examined the H1–H94–H98 interaction in the cryo-EM structures of a WT 70S ribosome (Watson et al. 2020) and ribosomes with an MS2-V2 tag (Nissley et al. 2023).
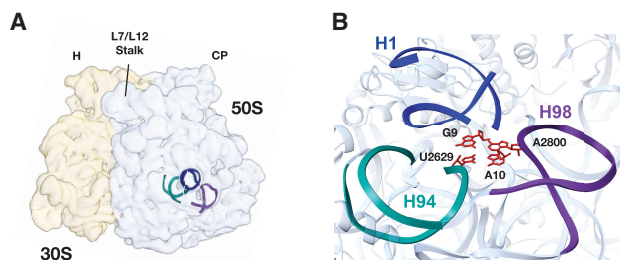

FIGURE 1. Location and overview of the region surrounding 23S rRNA helix H1. (*A*) Location of helices H1 (dark blue), H94 (teal), and H98 (purple) in the *E. coli* LSU. The locations of the central protuberance (CP) of the 50S subunit and head (H) of the 30S subunit are marked. (*B*) Structural model of the *E. coli* 70S ribosome (PDB:7K00) highlighting interactions between H1, H94, and H98. Nucleotides that form the interaction between these helices are colored red.
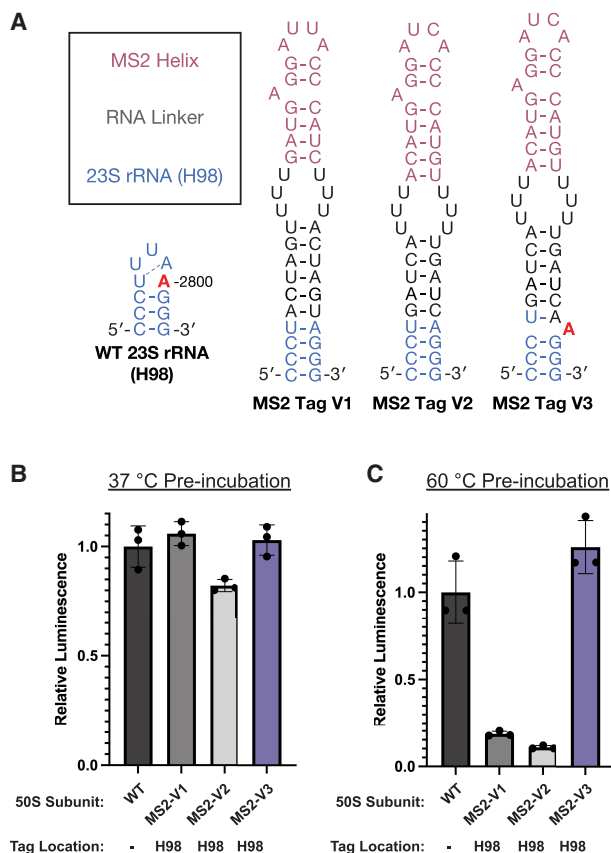
FIGURE 2. Design and activity of 50S subunits with MS2 tags inserted into H98. (*A*) The secondary structure of H98 in WT 23S rRNA or ribosomes with MS2 tags. The sequence of MS2-V1 and MS2-V2 are from Youngman and Green (2005) and Ward et al. (2019), respectively. Addition of an adenosine in MS2-V3 at a position equivalent to A2800 is proposed to mimic the sequence of the WT 23S rRNA (A2800 in red). 50S subunits were preincubated at (*B*) 37°C or (*C*) 60°C before their addition to the nanoLuciferase in vitro translation assay. Data are normalized to WT subunits with no MS2 tag. All error bars are the standard deviation of three experimental replicates.

In the WT ribosome, there is clear density for G9 (H1), A10 (H1), and U2629 (H94) sugars and bases. There is also clear density for the A2800 (H98) base despite poor density for the rest of the apical region of H98 (Fig. 3A), indicating that while H98 is dynamic on the surface of the ribosome, A2800 is rigidly docked through contacts with H1 nucleotides. In contrast, the ribosome with MS2-V2 inserted in H98, lacks density for A2800 and displays weak density for A10 suggesting that this nucleotide is more dynamic. While A2800 is not deleted in the MS2-V2 tag, the lack of density at its canonical position suggests that the adenosine forms a Watson–Crick base pair with U2796 in the H98 helix. The RNA helical extension of H98 in the MS2-V2 tag may energetically favor the A2800–U2796 base pair and force A2800 out of its canonical flipped position observed in the WT structure.

To determine how the addition of an adenosine residue in MS2-V3 affects the structure of the H1–H94–H98 region,

we determined the structure of an MS2-V3 tagged *E. coli* 70S ribosome with fMet-tRNA[fMet] in the P site to a global resolution of 1.8 Å. This high-resolution structure enabled the visualization of individual nucleotides on the surface of the ribosome, including some of those in H1 and H98 where local resolutions range from 2.2 to 2.4 Å (Supplemental Fig. S2). Additionally, we utilized 3D-variability analysis in cryoSPARC to better resolve the extended MS2 tag and could model the helix into lower-resolution helical density through the polyuridine stretch.

Although the apical MS2 helix and MS2 coat protein are likely too dynamic to be visualized, H98 with the MS2-V3 insertion adopts roughly the same conformation as WT H98, with the linker helix extending away from the surface of the 50S subunit (Fig. 3B). Importantly, there is clear density for both A10 and the additional adenosine at a position equivalent to 2800 in the WT ribosome (2833 with the MS2-V3 tag) (Fig. 3A). The additional adenosine is in a similar position to A2800 in the WT structure and forms similar hydrogen bonds with the other quartet nucleotides (Fig. 3B; Supplemental Fig. S3).

To further understand how the addition of the adenosine affects the extended H98, we looked at low-pass filtered maps for ribosomes with MS2-V2 and MS2-V3 tags (Fig. 3C). With MS2-V2 tags, there is a lack of density around the canonical location of A2800 and much of the linker helix, suggesting that once H1–H98 contacts are lost, H98 becomes highly dynamic. Upon the addition of an adenosine in MS2-V3 tags, there is a recovery of density for the extended H98. Thus, in the ribosome with an MS2-V3 tag, addition of an adenosine into the MS2 tag restores the H1–H94–H98 tertiary interaction and this recovers ribosome stability.

Nucleotide bridges between H1, H94, and H98 are required for full LSU stability

Since the interaction between H1, H94, and H98 plays a role in ribosome stability, we carefully examined the structure of this region. The nucleotide quartet is composed of two sets of base pairs which stack on one another: a type X *trans* Watson–Crick—sugar edge base pair between G9 and A2800 and a type XXIV *trans* Watson–Crick—Hoogsteen base pair between U2629 and A10. Additionally, N1 of G9 and N6 of A2800 interact with the 2′-OH of U2629 and G9, respectively (Fig. 4A).

To further interrogate the interactions between H1, H94, and H98, we inserted the MS2-V2 tag into H25, as a streptavidin binding aptamer was previously placed in H25 for the affinity purification of *E. coli* ribosomes (Leonov et al. 2003). By moving the MS2 tag into H25, we were able to maintain the WT sequence of H98 to determine how the native contacts in this region affect the stability of the LSU. The insertion of an MS2 tag into H25 has a slight negative effect on ribosome stability but no effect on activity at 37°C (Fig. 4B;
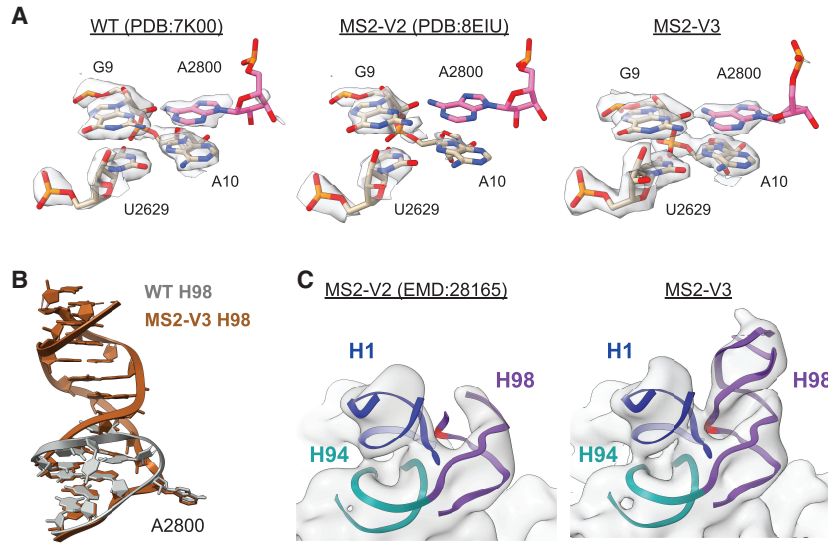
FIGURE 3. Structure of the *E. coli* 70S ribosome with MS2-V3 inserted in H98. (*A*) Model and density for the H1–H94–H98 nucleotide quartet in the WT 70S ribosome (*left*, PDB:7K00 EMD:22586), 70S ribosome with MS2-V2 inserted in H98 (*middle*, PDB:8EIU EMD:28165), and 70S ribosome with MS2-V3 inserted in H98 (*right*). Nucleotide A2800 is shown in pink and an additional *B*-factor of 15 Å² was applied to the cryo-EM maps. (*B*) Overview of H98 in the WT 70S ribosome (gray, PDB:7K00) and the helix upon insertion of MS2-V3 in H98 (brown). (*C*) Low-pass filtered cryo-EM maps for MS2-V2 (EMD:28165) and MS2-V3 overlaid on the MS2-V3 model for H1, H94, and H98. Cryo-EM maps were low-pass filtered to 10 Å. The nucleotide equivalent to A2800 (A2833) is marked in red.

pared to the other quartet mutations. It is likely that both nucleotides work together to fully link H1 to H94 and H98, and that the mutation of one residue does not completely abolish the interaction. Mutations to U2629 and A2800 led to the largest negative effects on ribosome stability. The mutation of these residues would prevent H94 or H98 from interacting with H1, which indicates that the loss of either of these contacts decreases ribosome stability. Subunits with an A2800U mutation had the lowest activity after pre-incubation at 60°C, suggesting that the H98–H1 interaction plays an important role in the stability of the *E. coli* LSU. When the nucleotides that base-pair (G9U) or base-stack (A10U) with A2800 are mutated, there is also a loss in ribosome stability. Additionally, a subunit with an A2800G mutation displayed slightly higher levels of activity after preincubation at 60°C than one with an A2800U mutation. The guanosine at position 2800 would still be able
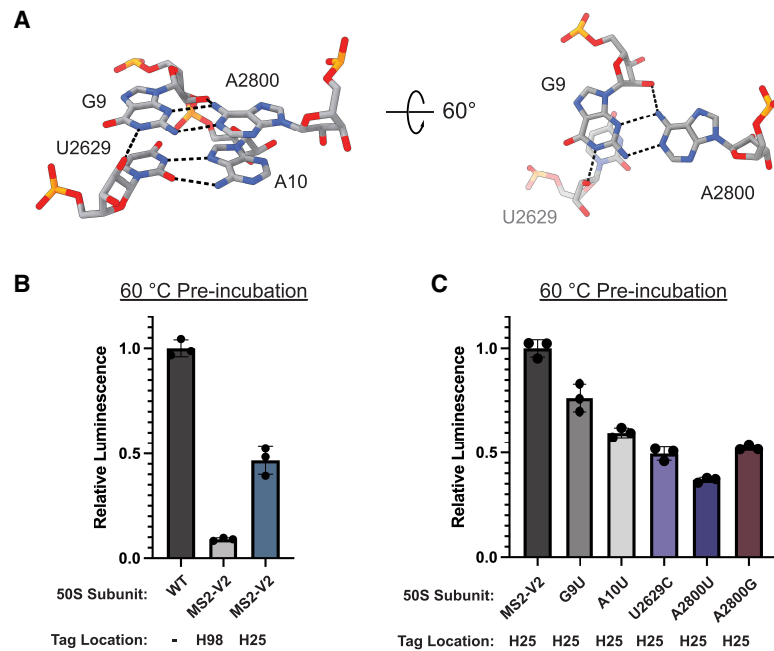
Supplemental Fig. S4). This result suggests that the extension of solvent-accessible helices on the surface of the ribosome can have unexpected effects on ribosome folding and stability. Utilizing the MS2 tag inserted into H25, the following 50S mutant subunits were purified: G9U, A10U, U2629C, A2800U, and A2800G. Purine to uridine mutations (G9U, A10U, and A2800U) were made to disrupt base-pairing and base-stacking in the H1–H94–H98 tertiary contact as uridine has higher (less favorable) base-stacking free energies than purine nucleotides (Frechet et al. 1979; Hayatshahi et al. 2018). A U2629C mutation was hypothesized to make minor perturbations to the U2629-A10 pair while maintaining the smaller pyrimidine ring size.

Mutations in the quartet nucleotides did not decrease ribosome activity at 37°C but negatively affected ribosome stability (Fig. 4C; Supplemental Fig. S4). The G9U and A10U mutant subunits had the highest stability com-

FIGURE 4. Base-pairing and stacking in the H1–H94–H98 nucleotide quartet. (*A*) Overview of the nucleotide quartet in the WT 70S ribosome. Hydrogen bonds between the bases and sugars are shown in black. (*B*) nLuc in vitro translation assay for WT (no tag), MS2-V2 inserted into H98, and MS2-V2 inserted into H25 after preincubation of 50S subunits at 60°C. Data are normalized to untagged 50S subunits. (*C*) nLuc in vitro translation assay for 50S subunits with MS2-V2 inserted into H25 and mutations in the H1–H94–H98 quartet after preincubation of 50S subunits at 60°C. Data are normalized to subunits with MS2-V2 inserted into H25. All error bars are the standard deviation of three experimental replicates.

to form a purine–purine base stack with A10 but would not be able to base-pair with the sugar edge of G9, indicating that base-stacking in this region likely plays an important role in nucleotide engagement.

H98 is a poorly conserved helix in 23S rRNA that is absent in ribosomes from many organisms (Matadeen et al. 2001). Since H1, H94, and H98 play a role in the stability of the *E. coli* LSU, we wondered whether these helices play similar roles in other bacterial ribosomes. We examined the region surrounding H1 in various high-resolution structures of bacterial ribosomes that contain H98 (Table 1; Kaminishi et al. 2015; Mishra et al. 2018; Halfon et al. 2019; Murphy et al. 2020; Crowe-McAuliffe et al. 2021a,b; Basu et al. 2022; Cui et al. 2022; Morgan et al. 2022; Syroegin et al. 2023). Out of the surveyed structures, the ribosomes from two organisms, *Pseudomonas aeruginosa* and *Enterococcus faecalis*, have interactions between H1, H94, and H98 that form the same structure as in the *E. coli* ribosome. However, other organisms possess diverse sets of contacts between these helices that differ from the ones found in *E. coli* (Supplemental Fig. S5). For example, the interactions between the helices are more expansive in *Mycobacterium tuberculosis* and *Thermus thermophilus* than in *E. coli*. *T. thermophilus* ribosomes utilize complex hydrogen bond networks and base-stacking that involves both the 5′ and 3′ strands of H1, to bridge H1 with H94 and H98 (Supplemental Fig. S5). This is suggestive of a stronger interaction that could be advantageous at the higher growth temperatures of *T. thermophilus*. In all of the surveyed ribosome structures, there are interactions between the 5′ strand of H1 and a variable nucleotide at the base of H94. However, H98 does not interact with H1 in many of the structures, such as in *B subtilis*. In these bacteria, the H1–H94 interaction or other compensating interactions may be sufficient for ribosome stability.

Previously, it was shown that some bacteria lose H1 during the maturation of the LSU and that the loss of H1 is correlated with the evolutionary loss of H98 (Shatoff et al. 2021). This finding hinted at an unknown synergistic role between the two helices and that H1 became redundant after the evolutionary loss of H98. It was hypothesized that H98 may play a role in protecting H1 from RNase cleavage (Shatoff et al. 2021), and our data suggest that H98 plays an additional role in stabilizing the ribosome through interactions with the 5′ strand of H1. As the ribosomes of many organisms lack H98 and some bacteria cleave H1 during LSU assembly, there may be compensating interactions that replace the H1–H94–H98 interaction in these ribosomes. For example, in the *Flavobacterium johnsoniae* ribosome, which lacks H1 in the mature LSU, the 5′ and 3′ ends of the 23S rRNA interact with L22 and L32, respectively (Jha et al. 2021). L22 and L32 form a protein–protein interaction in the *F. johnsonjae* ribosome, which may play a synonymous role to the H1–H94–H98 RNA–RNA interaction in *E. coli* as it bridges the 5′ and 3′ ends of 23S rRNA.

Here, we show that the insertion of MS2 tags into H98 of 23S rRNA in the *E. coli* LSU using an uninterrupted RNA double helical extension (Youngman and Green 2005; Ward et al. 2019) disrupts contacts between H1, H94, and H98 and destabilizes the LSU. It has been shown that affinity handles inserted into helices on the surface of the *E. coli* LSU can have negative effects on ribosome activity, assembly, and cellular growth (Leonov et al. 2003; Hesslein 2004). The affinity tag described here builds on an MS2 tag design that does not affect cellular growth or ribosome activity (Youngman and Green 2005) and now also achieves WT levels of stability. Additionally, the design principles outlined here can be applied to the placement of affinity tags in H98 of other bacterial LSUs, where maintenance

TABLE 1. Interactions between rRNA helices H1, H94, and H98 from bacterial ribosomes with known structures

Organism	Phylum	H1 interacting nucleotides	H94 interacting nucleotides	H98 interacting nucleotides
Escherichia coli	Pseudomonadota	G A	U	A
Pseudomonas aeruginosa	Pseudomonadota	G A	U	A
Actinetobacter baumannii	Pseudomonadota	A A	U	U
Thermus thermophilus	Deinococcota	U G (U)	A	A
Deinococcus radiodurans	Deinococcota	U A	A	-
Bacillus subtilis	Bacillota	U A	A	-
Listeria monocytogenes	Bacillota	U A	A	-
Staphylococcus aureus	Bacillota	U A	A	-
Enterococcus faecalis	Bacillota	G A	U	A
Mycobacterium tuberculosis	Actinomycetota	G U (A)	C	G
Mycolicibacterium smegmatis	Actinomycetota	U U	C	-

The identities of RNA nucleotides from these helices which interact are listed. H1 nucleotides on the 3′ strand of 23S rRNA are shown in parentheses.

of H1–H94–H98 interactions should be prioritized. Maintaining stability in the LSU could be important when studying ribosome mutations elsewhere that affect assembly, RNA folding, and global stability, since conferring additional instability from the MS2 affinity tag could lead to inactive ribosomes.

RNA intrinsically forms compact structures, and it has been shown that the 5′ and 3′ ends of long RNAs are in close proximity (Yoffe et al. 2011; Leija-Martínez et al. 2014; Lai et al. 2018), likely playing a role in RNA folding and stability. This observation has also been made for the termini of many proteins, and in certain proteins the loss of the amino-terminal–carboxy-terminal interaction leads to protein destabilization or unfolding (Krishna and Englander 2005). RNAs with compact structures, such as rRNA and other ribozymes, have closer end-to-end distances than RNAs with less stable structures (Vicens et al. 2018). While H1 bridges the 5′ and 3′ ends of 23S rRNA, additional interactions between the 5′ end of H1 and terminal helices H94 and H98 on the 3′ end likely work to further tether the ends of the 23S rRNA. The interactions between helices on the ends of 23S rRNA likely stabilize the fold of certain bacterial ribosomal LSUs and may more broadly represent a method for stabilizing the fold of highly structured RNAs.

MATERIALS AND METHODS

Cloning and plasmid design

A modified pLK35 plasmid (Douthwaite et al. 1989), containing a tac promoter followed by the rrnB operon, which encodes the MS2-tagged 23S rRNA, was used for mutagenesis. Point mutations, insertions, and deletions were made using either the Q5 Mutagenesis Kit (NEB) or the In-Fusion Cloning Kit (Takara Bio) and the corresponding primer sets (Supplemental Table S1). MS2 tags inserted in H98 were placed between 23S rRNA bases 2796 and 2800, with the concomitant removal of nucleotides 2797–2799. To insert an MS2 tag into H25, the MS2-V2 sequence was placed between 23S rRNA bases 544 and 549, with the removal of nucleotides 545–548. The following DNA sequences were inserted for each tag design:

MS2-V1: 5′-ACTAGTTTTGATGAGGATTACCCATCTTTACTAGT-3′
MS2-V2: 5′-GATCATTTACATGAGGATCACCCATGTTTTTGATC-3′
MS2-V3: 5′-GATCATTTACATGAGGATCACCCATGTTTTTGATCA-3′

Ribosome expression and purification

Mutant *E. coli* 50S ribosomal subunits were expressed and purified as previously described (Nissley et al. 2023). Briefly, *E. coli* NEB Express I^q cells were transformed with the corresponding pLK35 plasmid. Transformants were grown in 3 L of LB broth containing 100 µg/mL ampicillin at 37°C. Cultures were induced with 0.5 mM isopropyl β-D-1-thiogalactopyranoside once they reached $OD_{600} = 0.6$ and were incubated for an additional 3 h. Cells were

pelleted, resuspended in 50 mL buffer A (20 mM Tris-HCl pH 7.5, 100 mM NH_4Cl, 10 mM $MgCl_2$, 0.5 mM EDTA, 2 mM dithiothreitol [DTT]) with Pierce protease inhibitor (Thermo Fisher), and lysed by sonication. The lysate was clarified by centrifugation and then loaded onto a sucrose cushion containing 24 mL of buffer B (20 mM Tris-HCl pH 7.5, 500 mM NH_4Cl, 10 mM $MgCl_2$, 0.5 mM EDTA, 2 mM DTT) with 0.5 M sucrose and 17 mL of buffer C (20 mM Tris-HCl pH 7.5, 60 mM NH_4Cl, 6 mM $MgCl_2$, 0.5 mM EDTA, 2 mM DTT) with 0.7 M sucrose in Type 45 Ti tubes (Beckman-Coulter). Ribosomes were pelleted by centrifugation at 27,000 rpm (57,000g) for 16 h at 4°C. The pellets were then resuspended in dissociation buffer (buffer C with 1 mM $MgCl_2$), which dissociates 70S ribosomes into 30S and 50S subunits.

MS2-tagged 50S subunits were then purified using a maltose binding protein (MBP)–MS2 fusion protein, which was purified as previously described (Ward et al. 2019). A 5 mL MBP Trap column (Cytiva) at 4°C was washed with five column volumes (CV) of MS2-150 buffer (20 mM HEPES pH 7.5, 150 mM KCl, 1 mM EDTA, 2 mM 2-mercaptoethanol) and then 10 mg of MBP–MS2 protein was loaded slowly onto the column. The column was then washed with five CV of buffer A-1 (buffer A with 1 mM $MgCl_2$), and crude ribosomes were loaded onto the column. The column was washed with five CV of buffer A-1, 10 CV of buffer A-250 (buffer A with 250 mM NH_4Cl and 1 mM $MgCl_2$), and then tagged ribosomal subunits were eluted with a 10 CV gradient of 0–10 mM maltose in buffer A-1. The purified 50S subunits were concentrated in 100 kDa cut off spin filters (Millipore), quantified with an approximation of 1 $A_{260} = 36$ nM, and flash frozen in liquid nitrogen. WT untagged 30S and 50S ribosomal subunits were purified as previously described (Nissley et al. 2023).

Mutant ribosome purity assay

To determine the levels of WT untagged 50S subunit contamination after mutant ribosome purification, semiquantitative PCR was utilized as previously described (Ward et al. 2019) with adaptations. Roughly 50 pmol of purified mutant ribosomes were denatured at 95°C for 3 min. LiCl was added to a final concentration of 5 M to precipitate the rRNA, which was subsequently resuspended in RNase-free water. Primers MS2_H98_quant_R or MS2_H25_quant_R, for mutant ribosomes with MS2 tags in either H98 or H25, respectively, were used to reverse transcribe a region of 23S rRNA using AMV reverse transcriptase (Promega). The region of cDNA containing the MS2 tag was amplified via PCR using primer pairs MS2_H98_quant_F and MS2_H98_quant_R or MS2_H25_quant_F and MS2_H25_quant_R. PCR products were resolved on a 10% polyacrylamide-TBE gel (Invitrogen) and visualized with SYBR gold stain (Thermo Fisher). DNA bands were quantified with ImageJ software (Schneider et al. 2012).

In vitro nanoluciferase translation endpoint assay

50S subunits were diluted to 1.4 µM in buffer A with a final concentration of 10 mM $MgCl_2$. The diluted subunits were incubated for 15 min at the indicated temperature and then incubated for an additional 15 min at room temperature to cool. An in vitro translation reaction was then assembled using the PURExpress system (NEB) with the following: 3.2 µL solution A (NEB), 1 µL factor mix (NEB), 250 nM preincubated 50S subunit, 500 nM WT 30S

subunit, 1 U/μL RNase inhibitor (NEB), and 10 ng/μL of a plasmid containing a T7 promoter followed by the nLuc gene (final volume of 8 μL). The reaction was incubated for 1 h at 37°C and then 2 μL of the reaction was mixed with 30 μL of nLuc buffer (20 mM HEPES pH 7.5, 50 mM KCl, and 10% glycerol) and a 1:50 dilution of Nano-Glo substrate (Promega). All 32 μL were then placed in a 384-well plate and luminescence was measured in a Spark Plate Reader (Tecan). Experimental triplicates were measured and averaged for each in vitro translation reaction.

MetRS and MTF expression and purification

Plasmids containing a T7 promoter followed by the gene for *E. coli* methionyl-tRNA synthetase (MetRS) or methionyl-tRNA formyltransferase (MTF) and a 6×-His tag were transformed into *E. coli* BL21 (DE3) Codon+ RIL cells. Overnight cultures were diluted in ZYM-5052 autoinducing media (Studier 2014) and grown overnight at 37°C. Cells were then pelleted by centrifugation, resuspended in lysis buffer (20 mM Tris pH 7.8, 150 mM NaCl, 5 mM imidazole, 0.5 mM EDTA), and lysed by sonication. The lysate was clarified by centrifugation at 25,000g (JA-20 rotor, Beckman) at 4°C for 30 min. The supernatant was applied to a 5 mL HisTrap column (Cytiva) at 4°C and the column was washed with five CV of lysis buffer with 23 mM imidazole. Protein was eluted from the column using a linear gradient of 20 CV lysis buffer from 23 to 500 mM imidazole. The eluted protein was then dialyzed against 50 mM HEPES pH 7.5, 100 mM KCl, 10 mM $MgCl_2$, 7 mM β-mercaptoethanol (BME), and 30% glycerol, concentrated, and stored at −80°C.

fMet-tRNA^fMet preparation

tRNA^fMet with a C1G mutation and a modified terminal 3′-NH$_2$-ATP was in vitro transcribed and modified as previously described (Nissley et al. 2023). fMet-tRNA^fMet was prepared enzymatically as described (Walker and Fredrick 2008). Briefly, a charging reaction was prepared with the following: 10 μM NH$_2$-tRNA^fMet, 10 mM methionine, 300 μM N10-formyl-tetrahydrofolate, 10 mM ATP, 1 U/μL RNase inhibitor (NEB), 1 μM (MetRS), and 1 μM MTF in AA buffer (50 mM HEPES pH 7.5, 10 mM KCl, 20 mM $MgCl_2$, and 2 mM DTT). This reaction was incubated at 37°C for 30 min. The tRNA was then phenol–chloroform extracted, ethanol precipitated, and resuspended in water.

Cryo-EM sample preparation

An amount of 40 pmol of MS2-V3 50S subunit and 80 pmol WT untagged 30S subunit were incubated at 37°C in buffer C with a total of 10 mM $MgCl_2$ for 45 min. This mixture was then split and loaded on to four 15%–40% (w/v) sucrose gradients in buffer D [20 mM HEPES pH 7.5, 100 mM KCl, 10 mM Mg(OAc)$_2$]. Gradients were centrifuged at 97,000g for 16 h in a SW-41 rotor (Beckman-Coulter). An ISCO fractionation system was used to isolate the 70S fraction from each gradient (Supplemental Fig. S6). 70S factions were then combined, washed in buffer D, and concentrated in a 100 kDa cut off spin filter (Millipore).

An amount of 100 nM 70S ribosome, 1 μM fMet-tRNA^fMet, and 5 μM mRNA with the sequence 5′-GUAUAAGGAGGUAAA<u>AUG</u>UUC

UAACUA-3′ (IDT) were combined in Buffer D with 15 mM MgOAc and incubated at 37°C for 45 min. The fMet codon is underlined in the mRNA sequence. Three-hundred mesh R1.2/R1.3 UltraAu foil grids with a deposited layer of amorphous carbon were glow discharged in a PELCO easiGlow for 12 sec under a 0.37 mBar vacuum and with 25 mA current. Four microliters of the complex were then added to the grid, incubated for 1 min, and then the grid was touched to three successive 100 μL drops of buffer D. Grids were plunge-frozen in liquid ethane using a Vitrobot Mark IV at 4°C with 100% humidity and the settings blot force 4 and blot time 2 sec.

Cryo-EM data acquisition, image processing, and modeling

Data were acquired as previously described (Watson et al. 2020) with adaptations (Supplemental Table S2). Briefly, movies were collected on a 300 kV Titan Krios microscope with a BIO-energy filter and Gatan K3 camera. The super-resolution pixel size was set to 0.405 (physical pixel size of 0.81), and SerialEM (Schorb et al. 2019) was used to automate data collection. Movies were collected over a defocus range of −0.5 to −1.5 μm with an electron dose of 40 e⁻/Å^2 split over 40 frames. Image shift was used to collect movies in a 3 × 3 grid of holes with two movies collected per hole.

Raw movies were Fourier-cropped to the physical calibrated pixel size (0.8248 Å) and patch motion corrected in cryoSPARC 3 (Punjani et al. 2017). CTFFind4 (Rohou and Grigorieff 2015) was used to estimate the CTFs of micrographs and ones with poor estimated CTF fit were manually excluded. Micrographs were then split into exposure groups based on the 3 × 3 groups during image-shift collection. Particles were picked using the cryoSPARC template picker with 70S ribosome 2D templates generated in cryoSPARC. Particles were then extracted and Fourier-cropped to 1/8 of the box size, and 2D classification was performed in cryoSPARC using 100 classes. Junk particles were rejected, and a second round of 2D classification was performed to further remove the remaining junk particles. Selected particles were reextracted and Fourier-cropped to 1/4 of the box size and 3D classification was performed with heterogeneous refinement in cryoSPARC using a 70S ribosome map from Nissley et al. (2023). Classes containing features consistent with 70S ribosomes were combined and subjected to another round of 3D classification. Classes from the second round of 3D classification that refined to high resolution were combined, and particles from these classes were extracted at the full box size. The particles were then subjected to homogeneous refinement in cryoSPARC with per-particle defocus optimization, per-group CTF parameter optimization, and Ewald sphere correction. Focus refinements were run separately on the 50S and 30S subunits with local refinement in cryoSPARC (Supplemental Fig. S7). For modeling, a composite map was constructed by combining the maps from the 50S and 30S focused refinements. PDB 7K00 (Watson et al. 2020), which was used as an initial 70S ribosome model, was aligned to the composite map in ChimeraX (Pettersen et al. 2021). Real-space refinement in PHENIX (Liebschner et al. 2019) was used to refine the model, and the manual adjustments were made to the model as needed in COOT (Supplemental Table S3; Casañal et al. 2020). To better model the MS2 tag, particles

were Fourier-cropped to 1/2 the box size, and the region containing H1 and H98 was masked and subjected to 3D-variability analysis in cryoSPARC (Supplemental Fig. S7). Each of the volume series was inspected, and the map which contained the best density for the MS2 tag and showed characteristics of an RNA helix was selected. The MS2 tag was modeled into this map using secondary structure constraints in PHENIX.

DATA DEPOSITION

Atomic coordinates have been deposited with the Protein Data Bank under accession code 8FTO. Cryo-EM maps have been deposited with the Electron Microscopy Data Bank under accession codes EMD-29449 (composite map), EMD-29483 (70S global map), EMD-29484 (50S focused refinement map), and EMD-29485 (30S focused refinement map).

SUPPLEMENTAL MATERIAL

Supplemental material is available for this article.

ACKNOWLEDGMENTS

REFERENCES

Basu RS, Sherman MB, Gagnon MG. 2022. Compact IF2 allows initiator tRNA accommodation into the P site and gates the ribosome to elongation. *Nat Commun* **13:** 3388. doi:10.1038/s41467-022-31129-2

Casañal A, Lohkamp B, Emsley P. 2020. Current developments in *Coot* for macromolecular model building of electron cryo-microscopy and crystallographic data. *Protein Sci* **29:** 1055–1064. doi:10.1002/pro.3791

Crowe-McAuliffe C, Murina V, Turnbull KJ, Kasari M, Mohamad M, Polte C, Takada H, Vaitkevicius K, Johansson J, Ignatova Z, et al. 2021a. Structural basis of ABCF-mediated resistance to pleuromutilin, lincosamide, and streptogramin A antibiotics in Gram-positive pathogens. *Nat Commun* **12:** 3577. doi:10.1038/s41467-021-23753-1

Crowe-McAuliffe C, Takada H, Murina V, Polte C, Kasvandik S, Tenson T, Ignatova Z, Atkinson GC, Wilson DN, Hauryliuk V. 2021b. Structural basis for bacterial ribosome-associated quality control by RqcH and RqcP. *Mol Cell* **81:** 115–126.e7. doi:10.1016/j.molcel.2020.11.002

Cui Z, Li X, Shin J, Gamper H, Hou Y-M, Sacchettini JC, Zhang J. 2022. Interplay between an ATP-binding cassette F protein and the ribosome from *Mycobacterium tuberculosis*. *Nat Commun* **13:** 432. doi:10.1038/s41467-022-28078-1

Douthwaite S, Powers T, Lee JY, Noller HF. 1989. Defining the structural requirements for a helix in 23S ribosomal RNA that confers erythromycin resistance. *J Mol Biol* **209:** 655–665. doi:10.1016/0022-2836(89)93000-3

Frechet D, Ehrlich R, Remy P. 1979. Thermal perturbation differential spectra of ribonucleic acids. II. Nearest neighbour interactions. *Nucleic Acids Res* **7:** 1981–2001. doi:10.1093/nar/7.7.1981

Ginsburg D, Steitz JA. 1975. The 30 S ribosomal precursor RNA from *Escherichia coli*. A primary transcript containing 23 S, 16 S, and 5 S sequences. *J Biol Chem* **250:** 5647–5654. doi:10.1016/S0021-9258(19)41228-3

Halfon Y, Matzov D, Eyal Z, Bashan A, Zimmerman E, Kjeldgaard J, Ingmer H, Yonath A. 2019. Exit tunnel modulation as resistance mechanism of *S. aureus* erythromycin resistant mutant. *Sci Rep* **9:** 11460. doi:10.1038/s41598-019-48019-1

Hayatshahi HS, Henriksen NM, Cheatham TE. 2018. Consensus conformations of dinucleoside monophosphates described with well-converged molecular dynamics simulations. *J Chem Theory Comput* **14:** 1456–1470. doi:10.1021/acs.jctc.7b00581

Hesslein AE. 2004. Exploration of the conserved A+C wobble pair within the ribosomal peptidyl transferase center using affinity purified mutant ribosomes. *Nucleic Acids Res* **32:** 3760–3770. doi:10.1093/nar/gkh672

Jha V, Roy B, Jahagirdar D, McNutt ZA, Shatoff EA, Boleratz BL, Watkins DE, Bundschuh R, Basu K, Ortega J, et al. 2021. Structural basis of sequestration of the anti-Shine-Dalgarno sequence in the Bacteroidetes ribosome. *Nucleic Acids Res* **49:** 547–567. doi:10.1093/nar/gkaa1195

Kaminishi T, Schedlbauer A, Fabbretti A, Brandi L, Ochoa-Lizarralde B, He C-G, Milón P, Connell SR, Gualerzi CO, Fucini P. 2015. Crystallographic characterization of the ribosomal binding site and molecular mechanism of action of Hygromycin A. *Nucleic Acids Res* **43:** 10015–10025. doi:10.1093/nar/gkv975

Krishna MMG, Englander SW. 2005. The N-terminal to C-terminal motif in protein folding and function. *Proc Natl Acad Sci* **102:** 1053–1058. doi:10.1073/pnas.0409114102

Lai W-JC, Kayedkhordeh M, Cornell EV, Farah E, Bellaousov S, Rietmeijer R, Salsi E, Mathews DH, Ermolenko DN. 2018. mRNAs and lncRNAs intrinsically form secondary structures with short end-to-end distances. *Nat Commun* **9:** 4328. doi:10.1038/s41467-018-06792-z

Lancaster L, Lambert NJ, Maklan EJ, Horan LH, Noller HF. 2008. The sarcin–ricin loop of 23S rRNA is essential for assembly of the functional core of the 50S ribosomal subunit. *RNA* **14:** 1999–2012. doi:10.1261/rna.1202108

Leija-Martínez N, Casas-Flores S, Cadena-Nava RD, Roca JA, Mendez-Cabañas JA, Gomez E, Ruiz-Garcia J. 2014. The separation between the 5′-3′ ends in long RNA molecules is short and nearly constant. *Nucleic Acids Res* **42:** 13963–13968. doi:10.1093/nar/gku1249

Leonov AA, Sergiev PV, Bogdanov AA, Brimacombe R, Dontsova OA. 2003. Affinity purification of ribosomes with a lethal G2655C mutation in 23 S rRNA that affects the translocation. *J Biol Chem* **278:** 25664–25670. doi:10.1074/jbc.M302873200

Li Z, Pandit S, Deutscher MP. 1999. Maturation of 23S ribosomal RNA requires the exoribonuclease RNase T. *RNA* **5:** 139–146. doi:10.1017/S1355838299981669

Liebschner D, Afonine PV, Baker ML, Bunkóczi G, Chen VB, Croll TI, Hintze B, Hung L-W, Jain S, McCoy AJ, et al. 2019. Macromolecular structure determination using X-rays, neutrons and electrons: recent developments in *Phenix*. *Acta Crystallogr Sect Struct Biol* **75:** 861–877. doi:10.1107/S2059798319011471

Liiv A, Remme J. 1998. Base-pairing of 23 S rRNA ends is essential for ribosomal large subunit assembly. *J Mol Biol* **276:** 537–545. doi:10.1006/jmbi.1997.1532

Lowary PT, Uhlenbeck OC. 1987. An RNA mutation that increases the affinity of an RNA–protein interaction. *Nucleic Acids Res* **15:** 10483–10493. doi:10.1093/nar/15.24.10483

Matadeen R, Sergiev P, Leonov A, Pape T, van der Sluis E, Mueller F, Osswald M, von Knoblauch K, Brimacombe R, Bogdanov A, et al. 2001. Direct localization by cryo-electron microscopy of secondary structural elements in *Escherichia coli* 23 S rRNA which differ from the corresponding regions in *Haloarcula marismortui*. *J Mol Biol* **307**: 1341–1349. doi:10.1006/jmbi.2001.4547

Metelev M, Lundin E, Volkov IL, Gynnå AH, Elf J, Johansson M. 2022. Direct measurements of mRNA translation kinetics in living cells. *Nat Commun* **13**: 1852. doi:10.1038/s41467-022-29515-x

Mishra S, Ahmed T, Tyagi A, Shi J, Bhushan S. 2018. Structures of *Mycobacterium smegmatis* 70S ribosomes in complex with HPF, tmRNA, and P-tRNA. *Sci Rep* **8**: 13587. doi:10.1038/s41598-018-31850-3

Morgan CE, Zhang Z, Bonomo RA, Yu EW. 2022. An analysis of the novel fluorocycline TP-6076 bound to both the ribosome and multidrug efflux pump AdeJ from *Acinetobacter baumannii*. *MBio* **13**: e03732-21. doi:10.1128/mbio.03732-21

Murphy EL, Singh KV, Avila B, Kleffmann T, Gregory ST, Murray BE, Krause KL, Khayat R, Jogl G. 2020. Cryo-electron microscopy structure of the 70S ribosome from *Enterococcus faecalis*. *Sci Rep* **10**: 16301. doi:10.1038/s41598-020-73199-6

Nikolaev N, Silengo L, Schlessinger D. 1973. A role for ribonuclease III in processing of ribosomal ribonucleic acid and messenger ribonucleic acid precursors in *Escherichia coli*. *J Biol Chem* **248**: 7967–7969. doi:10.1016/S0021-9258(19)43281-X

Nissley AJ, Penev PI, Watson ZL, Banfield JF, Cate JHD. 2023. Rare ribosomal RNA sequences from archaea stabilize the bacterial ribosome. *Nucleic Acids Res* **51**: 1880–1894. doi:10.1093/nar/gkac1273

Noller HF. 2005. RNA structure: reading the ribosome. *Science* **309**: 1508–1514. doi:10.1126/science.1111771

Peabody DS. 1993. The RNA binding site of bacteriophage MS2 coat protein. *EMBO J* **12**: 595–600. doi:10.1002/j.1460-2075.1993.tb05691.x

Pettersen EF, Goddard TD, Huang CC, Meng EC, Couch GS, Croll TI, Morris JH, Ferrin TE. 2021. UCSF ChimeraX: structure visualization for researchers, educators, and developers. *Protein Sci* **30**: 70–82. doi:10.1002/pro.3943

Punjani A, Rubinstein JL, Fleet DJ, Brubaker MA. 2017. cryoSPARC: algorithms for rapid unsupervised cryo-EM structure determination. *Nat Methods* **14**: 290–296. doi:10.1038/nmeth.4169

Rohou A, Grigorieff N. 2015. CTFFIND4: fast and accurate defocus estimation from electron micrographs. *J Struct Biol* **192**: 216–221. doi:10.1016/j.jsb.2015.08.008

Schneider CA, Rasband WS, Eliceiri KW. 2012. NIH Image to ImageJ: 25 years of image analysis. *Nat Methods* **9**: 671–675. doi:10.1038/nmeth.2089

Schorb M, Haberbosch I, Hagen WJH, Schwab Y, Mastronarde DN. 2019. Software tools for automated transmission electron microscopy. *Nat Methods* **16**: 471–477. doi:10.1038/s41592-019-0396-9

Shajani Z, Sykes MT, Williamson JR. 2011. Assembly of bacterial ribosomes. *Annu Rev Biochem* **80**: 501–526. doi:10.1146/annurev-biochem-062608-160432

Shatoff EA, Gemler BT, Bundschuh R, Fredrick K. 2021. Maturation of 23S rRNA includes removal of helix H1 in many bacteria. *RNA Biol* **18**: 856–865. doi:10.1080/15476286.2021.2000793

Studier FW. 2014. Stable expression clones and auto-induction for protein production in *E. coli*. *Methods Mol Biol* **1091**: 17–32. doi:10.1007/978-1-62703-691-7_2

Syroegin EA, Aleksandrova EV, Polikanov YS. 2023. Insights into the ribosome function from the structures of non-arrested ribosome–nascent chain complexes. *Nat Chem* **15**: 143–153. doi:10.1038/s41557-022-01073-1

Vicens Q, Kieft JS, Rissland OS. 2018. Revisiting the closed-loop model and the nature of mRNA 5′-3′ communication. *Mol Cell* **72**: 805–812. doi:10.1016/j.molcel.2018.10.047

Walker SE, Fredrick K. 2008. Preparation and evaluation of acylated tRNAs. *Methods* **44**: 81–86. doi:10.1016/j.ymeth.2007.09.003

Ward FR, Watson ZL, Ad O, Schepartz A, Cate JHD. 2019. Defects in the assembly of ribosomes selected for β-amino acid incorporation. *Biochemistry* **58**: 4494–4504. doi:10.1021/acs.biochem.9b00746

Watson ZL, Ward FR, Méheust R, Ad O, Schepartz A, Banfield JF, Cate JH. 2020. Structure of the bacterial ribosome at 2 Å resolution. *Elife* **9**: e60482. doi:10.7554/eLife.60482

Yoffe AM, Prinsen P, Gelbart WM, Ben-Shaul A. 2011. The ends of a large RNA molecule are necessarily close. *Nucleic Acids Res* **39**: 292–299. doi:10.1093/nar/gkq642

Youngman EM, Green R. 2005. Affinity purification of in vivo-assembled ribosomes for *in vitro* biochemical analysis. *Methods* **36**: 305–312. doi:10.1016/j.ymeth.2005.04.007

Youngman EM, Brunelle JL, Kochaniak AB, Green R. 2004. The active site of the ribosome is composed of two layers of conserved nucleotides with distinct roles in peptide bond formation and peptide release. *Cell* **117**: 589–599. doi:10.1016/S0092-8674(04)00411-8